IJMMM International Journal of Minerals, Metallurgy and Materials 矿物冶金与材料学报（英文版）

A novel solution treatment and aging for powder bed fusion–laser beam Ti–6Al–2Sn–4Zr–6Mo alloy: Microstructural and mechanical characterization

Gianluca Pirro, Alessandra Martucci, Alessandro Morri, Mariangela Lombardi, and Lorella Ceschini

Cite this article as:
Gianluca Pirro, Alessandra Martucci, Alessandro Morri, Mariangela Lombardi, and Lorella Ceschini, A novel solution treatment and aging for powder bed fusion–laser beam Ti–6Al–2Sn–4Zr–6Mo alloy: Microstructural and mechanical characterization, *Int. J. Miner. Metall. Mater.*, 32(2025), No. 2, pp. 414-424. https://doi.org/10.1007/s12613-024-3006-5

INTERNATIONAL JOURNAL OF
Minerals, Metallurgy and Materials

Volume 32, Number 2, February 2025
Page 414

Research Article https://doi.org/10.1007/s12613-024-3006-5

A novel solution treatment and aging for powder bed fusion–laser beam Ti–6Al–2Sn–4Zr–6Mo alloy: Microstructural and mechanical characterization

Gianluca Pirro[1),✉], *Alessandra Martucci*[2)], *Alessandro Morri*[1)], *Mariangela Lombardi*[2)], *and Lorella Ceschini*[1)]

1) Department of Industrial Engineering (DIN), Alma Mater Studiorum – University of Bologna, Bologna 40136, Italy
2) Department of Applied Science and Technology (DISAT), Politecnico di Torino, Torino TO 10129, Italy
(Received: 21 June 2024; revised: 9 September 2024; accepted: 11 September 2024)

Abstract: Ti–6Al–4Zr–2Sn–6Mo alloy is one of the most recent titanium alloys processed using powder bed fusion–laser beam (PBF–LB) technology. This alloy has the potential to replace Ti–6Al–4V in automotive and aerospace applications, given its superior mechanical properties, which are approximately 10% higher in terms of ultimate tensile strength (UTS) and yield strength after appropriate heat treatment. In as-built conditions, the alloy is characterized by the presence of soft orthorhombic α″ martensite, necessitating a postprocessing heat treatment to decompose this phase and enhance the mechanical properties of the alloy. Usually, PBFed Ti6246 components undergo an annealing process that transforms the α″ martensite into an α–β lamellar microstructure. The primary objective of this research was to develop a solution treatment and aging (STA) heat treatment tailored to the unique microstructure produced by the additive manufacturing process to achieve an ultrafine bilamellar microstructure reinforced by precipitation hardening. This study investigated the effects of various solution temperatures in the α–β field (ranging from 800 to 875°C), cooling media (air and water), and aging time to determine the optimal heat treatment parameters for achieving the desired bilamellar microstructure. For each heat treatment condition, different α–β microstructures were found, varying in terms of the α/β ratio and the size of the primary α-phase lamellae. Particular attention was given to how these factors were influenced by increases in solution temperature and how microhardness correlated with the percentage of the metastable β phase present after quenching. Tensile tests were performed on samples subjected to the most promising heat treatment parameters. A comparison with literature data revealed that the optimized STA treatment enhanced hardness and UTS by 13% and 23%, respectively, compared with those of the annealed alloy. Fracture surface analyses were conducted to investigate fracture mechanisms.

Keywords: powder bed fusion–laser beam; titanium alloys; heat treatments; mechanical properties; fractographic analysis

1. Introduction

Titanium alloys are widely used in the transportation sector, especially in automotive and aerospace applications, because of their remarkable combination of strength and lightweight properties, excellent corrosion resistance, and high mechanical properties both at room and elevated temperatures [1–3].

Titanium is an allotropic element with a hexagonal closed-pack lattice at temperatures up to 883°C (α phase) and a body-centered cubic lattice (β phase) at temperatures higher than 883°C. Alloying elements can stabilize either the α or β phases, leading to the classification of titanium alloys based on phase proportions at room temperature: α alloys (β phase < 5%), α–β alloys (β phase < 20%), and β alloys (β phase > 30%) [2,4–5]. Among various titanium alloys, Ti–6Al–4V (Ti64), belonging to the α–β alloy family, stands out as the most widely used in industrial environments, accounting for over 50% of the total titanium production [1]. Nevertheless, Ti–6Al–2Sn–4Zr–6Mo (Ti6246), the α–β alloy with a higher percentage of β-stabilizers, has replaced the Ti64 alloy in applications demanding high strength, good creep, and oxidation resistance at elevated operating temperatures, such as in compressor discs and brakes for aero engines [6–7].

Traditionally, Ti alloy components are manufactured using plastic deformation, welding, and machining processes. However, the increasing demand for high-performance components with complex geometries, combined with the challenges of machining titanium using traditional methods, has led to the exploration of titanium alloys in additive manufacturing (AM) processes [8–10]. AM enables the production of components with increased flexibility and freedom, mitigating challenges associated with traditional machining. In particular, the powder bed fusion–laser beam (PBF–LB) techno-

✉ Corresponding author: Gianluca Pirro E-mail: gianluca.pirro2@unibo.it

logy facilitates the production of near-net-shape structures directly from computer-aided design models, significantly decreasing the necessity for rough machining and thereby reducing the "buy-to-fly" ratio [10]. In addition, the optimized design of structural components can contribute to weight reduction that, in the transportation field, can result in improved fuel efficiency, reduced greenhouse gas emissions, and longer battery life [11–12].

PBF–LB is a layer-by-layer process that exploits a focused laser beam to selectively melt and fuse metal powder particles. The process features rapid heating and cooling rates (up to 10^8 K/s [13]), much higher than those in conventional process (up to 10^2–10^3 K/s). This rapid thermal cycling results in very fine microstructures with nonequilibrium compositions [13–15]. Melt pools, induced by the local fusion of the powders, are among the typical microstructural features of PBF–LB metal alloys. The rapid cooling rates and directional thermal gradients also form columnar prior β grains that cross the melt pool borders. Within these β grains, the high content of β stabilizers leads to the development of acicular orthorhombic martensite α″ [7,16]. This martensite exhibits a softer behavior than that of the hexagonal hard α′ martensite usually observed in α–β PBF–LB alloys, such as Ti64 [9,13,17], in the as-built condition. However, despite its worsening effects on hardness and tensile strength, as the literature proves, α″ martensite leads to important improvements in ductility. Given the high residual stresses in as-built PBF–LB titanium alloys because of high heat inputs and low thermal conductivity [18–19], developing tailored heat treatments to fully exploit the potential of the PBF–LB Ti6246 alloy is crucial.

On the basis of the literature related to conventional-wrought Ti6246 alloy [20–22], a solution treatment and aging (STA) treatment is usually performed after the thermomechanical deformation process to induce the highest strength. According to Cotton *et al.* [23], the best performance can be achieved when the microstructure post-solution treatment consists of an oversaturated β phase without martensite. For α–β alloys with a high β-stabilizer content like Ti6246, the solution treatment is generally performed just below the β-transus (T_β) to limit β-grain growth and achieve an optimal strength–ductility balance after aging [24]. The aging treatment, typically conducted within a temperature range of 450 to 650°C, leads to the partial transformation of the metastable bcc β-phase and the subsequent formation of the equilibrium secondary hcp α-phase [20–21], resulting in a bimodal microstructure. The bimodal microstructure is notably characterized by globular primary α particles embedded within a lamellar secondary α and β retained matrix [5,25]. Because of a fundamental difference in their microstructure, the STA treatment parameters applied to the plastically deformed alloy cannot be directly applied to the alloy produced via the PBF–LB process. Whereas the plastically deformed alloy exhibits a coarse lamellar α–β structure [26–27], the PBFed alloy shows a metastable martensitic structure. Therefore, the solution treatment temperature and time must be carefully considered to ensure complete transformation of the initial martensitic structure and attainment of equilibrium phases, with proper morphology and amount, before quenching.

However, to the best of the authors' knowledge, no studies have explored the effects of STA on PBF–LB Ti6246 alloy to date. A previous work [16] examined the microstructural evolution of an as-built alloy following annealing with slow furnace cooling, which transformed α″ martensite into a coarse lamellar α–β structure, with small secondary α lamellae present within the β phase. However, the absence of the supersaturated β phase due to the slow cooling after annealing did not allow the precipitation hardening of the alloy. Meanwhile, despite the lack of published studies on the application of STA treatment to Ti6246 samples produced using PBF–LB, STA heat treatment has been extensively explored for other titanium α–β alloys manufactured using the PBF–LB technology, such as Ti64 [28–29] and near-α Ti6242 [30–31]. In this regard, Ter Haar and Becker [29] studied the PBF–LB Ti64 alloy and reported that annealing performed slightly below β-transus followed by water quenching generated a microstructure of coarse primary α lamellae separated by α′ martensite. The aging treatment transformed the α′ martensite into fine secondary α lamellae and β phase, resulting in the development of a bilamellar microstructure. Furthermore, it induced the precipitation of the strengthening Ti_3Al intermetallic phase. The presence of the fine secondary α lamellae and the Ti_3Al precipitates hindered dislocation slip [32], thereby enhancing mechanical properties of the Ti64 alloy compared with those of other microstructures while maintaining excellent ductility.

Given these previous considerations, this study aimed to optimize an STA heat treatment specifically tailored to the distinctive microstructure generated by the PBF–LB process on the Ti6246 alloy. In particular, several combinations of STA heat treatment parameters were explored to achieve a bilamellar microstructure, striking an optimal trade-off between tensile strength and ductility. This research examined solution temperatures within the α–β field (ranging from 800 to 875°C), different cooling media (air and water), and several temperature–time combinations of the aging treatments. The most promising heat treatments, identified through microstructural analysis and microhardness evaluation, were further tested for tensile strength. Analyses of stress–strain curves and fracture surfaces led to the identification of an STA treatment that reached an excellent compromise between strength and ductility.

2. Experimental

2.1. Samples production

A commercial gas-atomized Ti6246 powder, supplied by TLS Technik GmbH, was used as feedstock material for PBF–LB sample production. The powder chemical composition provided by the supplier compared with the standard (UNS R56260) [33] is reported in Table 1.

Table 1. Ti6246 chemical composition by the supplier and standard wt%

Sample	Ti	Al	Sn	Zr	Mo	Fe	C	N	O	H	Others
Supplier composition	Bal.	5.96	1.85	3.67	5.89	0.031	0.01	0.005	0.118	0.002	<0.30
UNS R56260 [33]	Bal.	5.5 ÷ 6.5	1.75 ÷ 2.25	3.5 ÷ 4.5	5.5 ÷ 6.5	Max. 0.15	Max. 0.04	Max. 0.04	Max. 0.15	Max. 0.125	Each max. 0.1 Total max. 0.4

The particle size distribution of the powder was analyzed using laser granulometry, yielding statistical parameters with D10, D50, and D90 values of 24.1, 38.0, and 54.7 μm, respectively.

The samples used in this study were produced using an EOS M270 Dual Mode 3D under a high-purity argon atmosphere. The machine was equipped with a continuous Nd:YAG fiber laser that could deliver up to 200 W of power, with a laser spot diameter of 100 μm. The PBF–LB process parameters, summarized in Table 2, were applied following an optimization study conducted previously [7].

2.2. Heat treatment and post-processing

To investigate the effects of different heat treatments on the microstructural and mechanical properties of the Ti6246 alloy, cubic samples measuring 15 mm × 15 mm × 15 mm and cylindrical samples with a height of 120 mm and a diameter of 12 mm were produced, as illustrated in Fig. 1(a). As shown in Fig. 1(a), the tensile test specimens were oriented vertically along the *z*-axis during printing, a common practice in industrial settings to maximize productivity and minimize support material usage. In addition, this orientation ensures the evaluation of the best-case scenario for the tensile tests as the load is applied parallel to the build direction, which is typically associated with the highest tensile strength due to the columnar nature of the β grains formed during the PBF–LB process. After production via PBF–LB, the samples were separated from the build platform, as shown in Fig. 1(b), using an electrical discharge machine to ensure precision and minimize thermal distortion. The heat treatments were conducted in a muffle furnace (Nabertherm LT 9/14) in an uncontrolled atmosphere, with samples either water-quenched or air-cooled. Because titanium alloys tend to oxide in the air when heated to above 480°C, forming a hard and brittle layer enriched with oxygen (referred to as the α case) [34], the tensile specimens were obtained by machining to completely remove the α case. Fig. 1(c) provides the geometry of the specimens defined according to BS EN ISO 6892-1:2019, whereas Fig. 1(d) shows an example of postmachining specimen.

X-ray diffraction (XRD) analyses were performed using a PANalytical X-Pert Philips diffractometer on *XZ* cross-sectioned samples to assess the effect of different heat treatments on both the phases present in the alloy and their crystallographic parameters. The analyses were recorded at 40 kV and 40 mA in a Bragg Brentano configuration using Cu K_α radiation. A step size of 0.013° and a 2θ range between 20° and 70° were considered.

The heat treatment optimization was conducted in two stages. In the first stage, the effects of the solution temperature and cooling conditions on hardness and microstructure were evaluated, with the aging temperature and time held constant. In the second stage, the impact of varying aging times was investigated. The solution temperatures explored ranged from 800 to 875°C, deliberately kept below the β-transus and the martensite start temperature (M_s) (above

Table 2. PBF–LB process parameters

Power / W	Scanning speed / (mm·s^{-1})	Hatch distance / μm	Layer thickness / μm	Scanning strategy	Platform temperature / °C
190	1250	100	30	Standard 67° EOS strategy	100

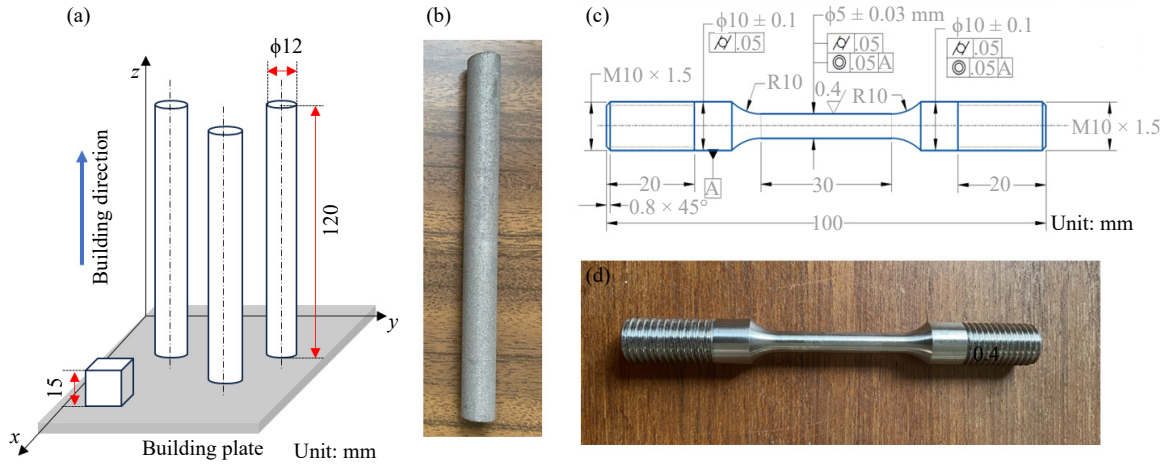

Fig. 1. (a) Graphical representation of the specimen set-up with orientations and dimensions, (b) photograph of the printed tensile sample, (c) technical drawing following the BS EN ISO 6892-1:2019 standard, and (d) sample after machining.

880°C, according to previous studies [35–36]) to prevent the formation of α′ and α″ martensite during cooling. The solution duration was set at 2 h, as in a previous study [16], with subsequent cooling conducted in both water and air. Final aging was performed at 500°C for durations ranging from 1 to 8 h. The literature commonly reported that high aging temperatures (600°C or above) for relatively long durations (6–8 h) have usually been used for the Ti6246 alloy [22,27,35]. However, as suggested by Vahidshad and Khodabakhshi [37], increasing the temperature above 500°C results in the formation of large precipitates, particularly Ti_3Al, which exhibit a limited hardening effect. Therefore, preliminary tests not included in the present study were conducted to identify the most suitable aging temperature. These tests corroborated the findings of Vahidshad and Khodabakhshi [37], confirming that 500°C was indeed the optimal aging temperature.

Table 3 summarizes all the treatment conditions investigated. The acronym used for each sample follows the format SolCM_Ag_Agh, where Sol = solution temperature, °C, CM = cooling mode (WQ = water quenching, AC = air cooling, and FC = furnace cooling), Ag = aging temperature, °C, and Agh = aging time, h.

Table 3. Heat treatment conditions tested on PBFed Ti6246 alloy

Heat treatment acronym	Solution temperature / °C	Solution time / h	Cooling condition	Aging temperature / °C	Aging time / h
800WQ_500_3	800	2	Water quenching	500	3
825WQ_500_3	825	2	Water quenching	500	3
850WQ_500_3	850	2	Water quenching	500	3
875WQ_500_3	875	2	Water quenching	500	3
875AC_500_3	875	2	Air cooling	500	3
875WQ	875	2	Water quenching	—	—
875FC	875	2	Furnace cooling	—	—
875WQ_500_1	875	2	Water quenching	500	1
875WQ_500_2	875	2	Water quenching	500	2
875WQ_500_4	875	2	Water quenching	500	4
875WQ_500_5	875	2	Water quenching	500	5
875WQ_500_6	875	2	Water quenching	500	6
875WQ_500_7	875	2	Water quenching	500	7
875WQ_500_8	875	2	Water quenching	500	8

2.3. Microstructural and mechanical characterization

Microstructural analyses and microhardness tests were conducted on *XZ* cross-sectioned samples. The metallographic preparation included hot mounting, grinding with abrasive papers up to 1200 grit, polishing with a diamond suspension (9 and 3 μm) and a water-based solution of colloidal silica and oxygen peroxide, and, finally, etching with Kroll reagent (93% H_2O, 5% HNO_3, and 2% HF) [38]. Low-magnification images of polished sections were acquired using a Zeiss Axio Imager A.1M optical microscope (OM), whereas high-magnification images were obtained using a Tescan Mira 3 field-emission scanning electron microscope (FE-SEM). Microstructural feature measurements were conducted using the ImageJ software, which distinguished between the two phases based on grayscale intensity. A threshold was applied to convert the image into a binary format, where the software identified the primary α phase lamellae as white regions. These regions were then approximated as ellipses, allowing the software to evaluate their geometric characteristics. The thickness of the primary α lamellae was calculated as the value of the minor diagonal of the ellipse that best approximated the single lamella [39] through image analysis processing, as demonstrated in Fig. 2. The α/β ratio was calculated by comparing the areas of the white regions (α phase) with those of the dark regions (β phase) [29]. To ensure a statistically robust estimation, ten images were analyzed for each heat treatment condition using the ImageJ software, with an average of 250 primary α phase lamellae measured per image.

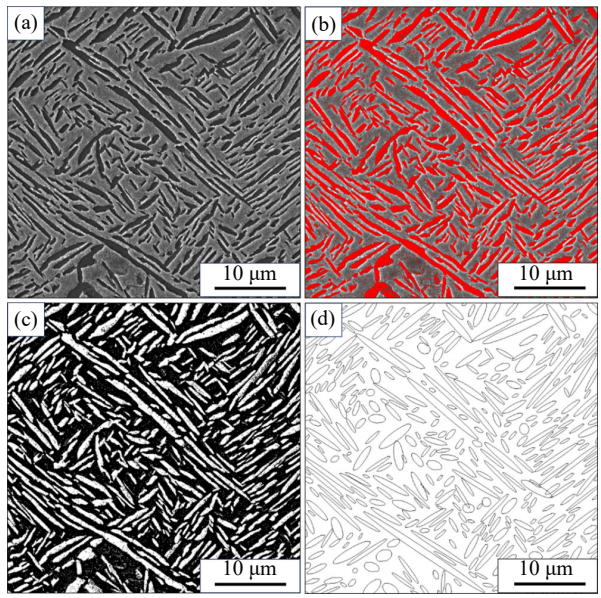

Fig. 2. Examples of image analysis processing paths comprising (a) the original FE-SEM image, (b) identification of the primary α lamellae using a threshold function, (c) conversion into a binary image, and (d) ellipse approximation of the α lamellae.

Microhardness tests were performed using a Vickers microhardness tester, Galileo Isoscan, with an applied load of 300 g for 15 s ($HV_{0.3}$).

Tensile tests were conducted following the ISO 6892-1:2019 standard using a servo-hydraulic testing machine to evaluate Young's modulus (E), yield strength (YS), ultimate tensile strength (UTS), and elongation after fracture (EL). Two sets of samples were tested: the first underwent the heat treatment 825WQ_500_3, and the second underwent the heat treatment 875WQ_500_3. The results of the tensile tests were compared with those of the 875FC samples, as reported previously [16].

3. Results and discussion

3.1. Heat treatment optimization and microstructure

Porosity analyses conducted using image analysis on both as-built and heat-treated samples revealed no substantial variations in porosity levels across different heat-treatment parameters, indicating that the observed porosity values primarily originated from the PBF–LB printing process. Cross-sectional analysis identified defects with sizes ranging from 10 to 150 μm. The average density in the *XY* cross-section was (99.84 ± 0.09)%, whereas it was (99.87 ± 0.05)% in the *XZ–YZ* longitudinal section. Most defects were small, circular in morphology, and indicative of gas porosity, as shown in Fig. 3(a). Larger defects, depicted in Fig. 3(b), characterized by irregular morphology and associated with lack of fusion (LoF), were also observed but were notably few.

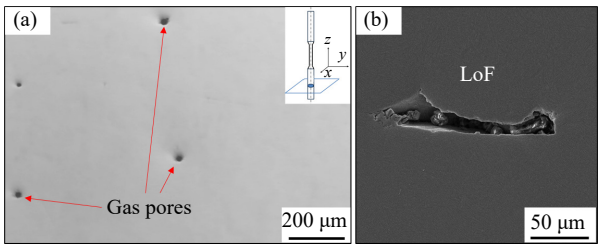

Fig. 3. (a) OM image of the analyzed *XY* cross-section and (b) FE-SEM image of an LoF defect.

Accurate OM and FE-SEM image analyses allowed the investigation of the Ti6246 PBF–LB as-built microstructure. According to Carrozza *et al.* [7], the as-built microstructure of the Ti6246 alloy exhibited characteristic features of PBF–LB-produced α–β titanium alloys: columnar prior-β grains aligned along the build direction, visible melt pools, and α″ martensitic needles (Fig. 4).

As previously reported, the formation of α″ martensite, although beneficial for ductility, has a detrimental effect on hardness and tensile strength because of its softer orthorhombic structure. Therefore, this martensite must be transformed through tailored heat treatment processes to enhance its mechanical properties, specifically by promoting the formation of more stable and harder phases, such as the α-phase or α + β microstructures, which contribute to improved hardness and strength in PBF–LB Ti6246 alloys [7,16].

In particular, the proper selection of solution temperatures

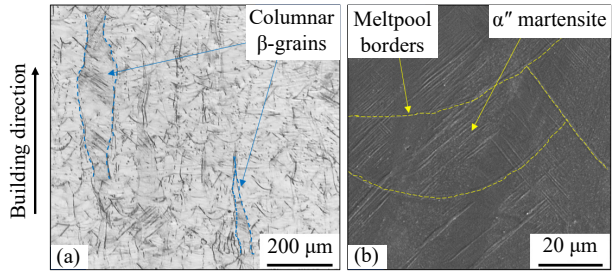

Fig. 4. Ti6246 PBF–LB as-built microstructure: (a) low-magnification OM image with visible columnar β-grains; (b) high-magnification FE-SEM image revealing α″ martensitic needles crossing melt pools.

and cooling rates is crucial for achieving both an ultrafine bilamellar microstructure and precipitation hardening after aging. The solution treatment transforms the α″ martensite into α lamellae and β phases. This is conducted in the α–β field at a temperature near the β-transus (~935°C for the Ti6246 alloy [35]). A higher solution temperature results in a lower ratio of α/β phases and thicker α lamellae. Thus, the identification of the best trade-off between the amount of the β phase and the size of the α lamellae is crucial for obtaining a high-performance bilamellar microstructure. A low amount of ultrafine secondary lamellae microstructures formed from the β phase leads to reduced mechanical properties. According to Kolli and Devaraj [21], in α–β alloys with a higher number of β-stabilizer elements, the formation of orthorhombic α″ martensite and hcp α′ martensite must be effectively suppressed during solution treatment and subsequent cooling. This allows the alloy to maintain a predominant retained body-centered cubic (bcc) β-phase microstructure and undergo precipitation hardening during aging. Therefore, water quenching or high-pressure gas quenching is necessary after solution treatment.

XRD analyses were conducted on a sample subjected to single treatment (875WQ) and on a sample after STA (875WQ_500_3) to verify the transformation of the martensitic phase and identify the phases present after heat treatment. The absence of the peaks corresponding to α″ martensite [16] for the sample 875WQ in the XRD diffraction pattern (Fig. 5) suggested its complete transformation. This finding agrees with previous studies [35–36], which reported that the formation of α″ martensite occurred during the quenching phase after a solution treatment above 880–900°C. Moreover, the XRD analyses suggested the absence of α′ martensite. In fact, despite sharing a hexagonal crystal structure and producing similar XRD reflections, α′ martensite can be differentiated from the α phase because of its noticeably broader peak widths [35,40]. Therefore, if α′ martensite was present after solution and quenching, the broad XRD reflections of the sample 875WQ should be different from that of the 875WQ_500_3 sample, which underwent aging and, therefore, did not have α′ martensite. Moreover, the 875WQ_500_3 sample consistently exhibited the presence of both α and β phases, similar to the unaged condition. However, a significant reduction in the main peak of the β phase, corresponding to a 2θ angle of ~39°, was evident for the 875WQ_

500_3 sample, highlighting a clear dominance of the α phase. Overlaying the two spectra, as shown in the inset of Fig. 5, the peaks of the 875WQ_500_3 sample clearly shifted to the right compared with those of the 875WQ sample. This shift could be attributed to the relaxation of stresses induced by the water-quenching treatment and the formation of strengthening precipitates during aging.

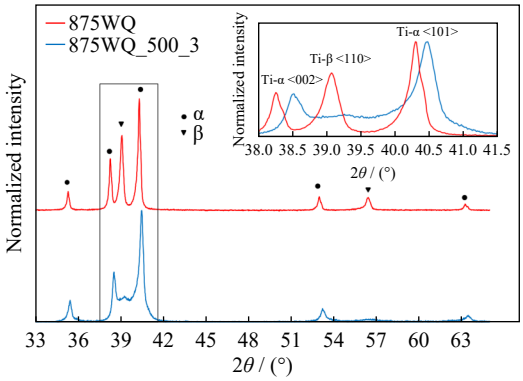

Fig. 5. XRD patterns of the 875WQ (red) and 875WQ_500_3 (blue) samples.

The results of the XRD analyses were confirmed by microstructural analyses conducted using FE-SEM. Fig. 6(a) and (b) depicts the microstructure of the 875WQ condition. The micrographs show the columnar β grains induced by the PBF–LB printing process within a lamellar microstructure (Widmanstätten pattern) of stable α lamellae and a metastable β-phase, confirming the absence of martensitic (needle-like) microstructures. The microstructure of the 875WQ_500_3 sample in Fig. 6(c) reveals a transformation of the metastable β phase of the 875WQ sample into a finely dispersed lamellar microstructure during the aging process. This microstructure consisted of secondary α lamellae embedded within a β matrix. These results were consistent with the previously discussed XRD analyses.

Fig. 7 shows the microstructures of the alloy after 800WQ_500_3, 825WQ_500_3, 850WQ_500_3, 875WQ_500_3, and 875AC_500_3 heat treatments. The 800WQ_500_3 treatment led to a very fine α–β lamellar structure, where the formation of secondary lamellae within the β-phase was not detectable. This peculiarity was instead easily visible, at the same magnification, in the microstructure of the samples 825WQ_500_3, 850WQ_500_3, and 875WQ_500_3. As depicted in Fig. 7(e), cooling from the solution temperature of 875°C using air as a quenching medium (875AC_500_3) also resulted in the formation of a bilamellar microstructure.

Fig. 8 shows the microstructure of samples annealed in the α–β field at 875°C for 2 h and furnace-cooled (875FC), as recommended by Carrozza *et al.* [16]. In this study, 875FC was regarded as the benchmark heat treatment as it offered a balanced combination of mechanical properties, as reported previously [16].

The above microstructure exhibited coarse primary α lamellae and small regions with secondary α lamellae. The secondary α lamellae, developed within the β-phase between the primary α lamellae, were significantly coarser than those observed in the bilamellar microstructure obtained with the STA treatments.

Fig. 9(a) illustrates the α/β ratio and the thickness of α laths measured across different samples as a function of solution temperature and cooling method (CM) after solution treatment. Focusing on the WQ samples, a clear trend emerged with increasing solution temperature, resulting in an enlargement of the primary α lamellae and a decrease in the α/β ratio. This trend aligned with the observations of Ter Haar and Becker [29] for the PBF–LB Ti64 alloy. The amount of retained β phase after quenching was crucial as its decomposition during aging led to the formation of secondary α-phase lamellae, significantly impacting the alloy's hardness. As shown in Fig. 9(b), the hardness increased directly with the percentage of the retained β phase.

Given that the 875WQ_500_3 sample exhibited the highest hardness after aging and developed a bilamellar microstructure, the aging time optimization was performed on samples solution-treated at 875°C. Before fine-tuning the aging conditions, the effect of the cooling rate on the micro-

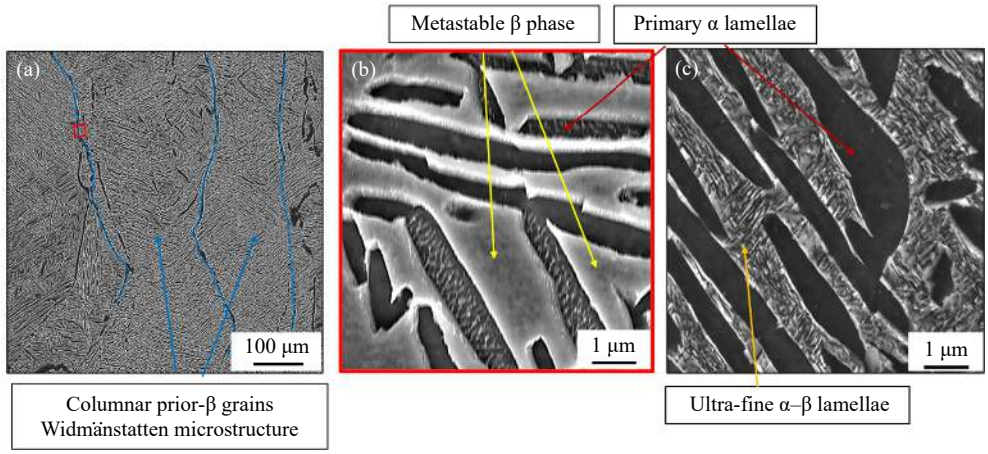

Fig. 6. (a) Low magnification of the 875WQ microstructure with clearly visible columnar prior-β grains, (b) high magnification of 875WQ showing a lamellar microstructure composed by stable primary α lamellae and a metastable β phase, and (c) high magnification of the 875WQ_500_3 sample highlighting the transformation of the metastable β phase into ultrafine α–β lamellae.

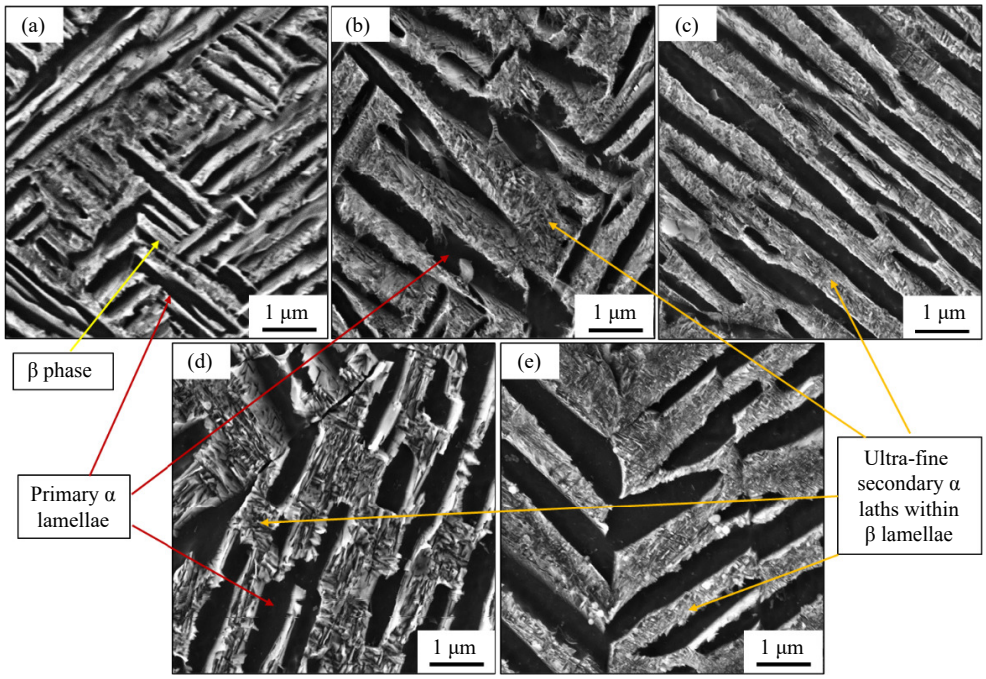

Fig. 7. FE-SEM images of (a) 800WQ_500_3, (b) 825WQ_500_3, (c) 850WQ_500_3, (d) 875WQ_500_3, and (e) 875AC_500_3 samples.

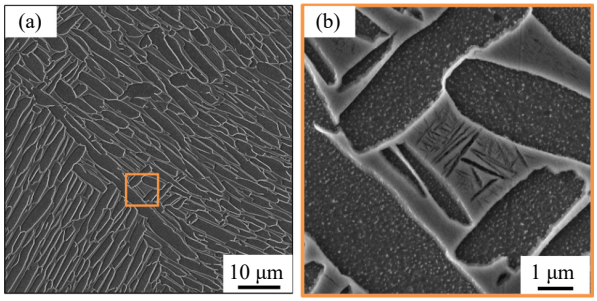

Fig. 8. FE-SEM images of the 875FC sample at (a) low and (b) high magnification.

structural and mechanical properties was analyzed. Notably, Fig. 9 highlights that the 875AC_500_3 sample exhibited reduced microhardness due to the lower percentage of metastable β phase available for transformation during aging, as well as the coarser microstructure characterized by thickened α laths. This outcome was consistent with the findings of Galarraga *et al.* [41], who observed a similar behavior in the Ti64 alloy and concluded that water quenching is the most effective method for achieving the desired strengthening effect.

For the 875FC samples, the α lamellae size was 1.54 μm, and the α/β ratio was 72.1%, which agreed with previous findings [16]. These values were notably higher than those observed in the 875WQ_500_3 sample, which had an average α lamellae size of 0.64 μm and a phase percentage ratio of 31.1%.

The coarser microstructure observed in the 875FC samples resulted from the slower cooling rate following the solution treatment, as the annealing temperature and time were identical to those used during the solution treatment. This slower cooling rate also led to a significant reduction in hardness (~20%) in the 875FC sample compared with the 875WQ_500_3 sample, attributed to the absence of strengthening precipitates and the larger size of the secondary α lamellae embedded within the β phase.

Fig. 10 reports both the aging curve of the alloy at 500°C and the microstructures of the alloy after different aging times. The peak aged condition was reached after 2 h of

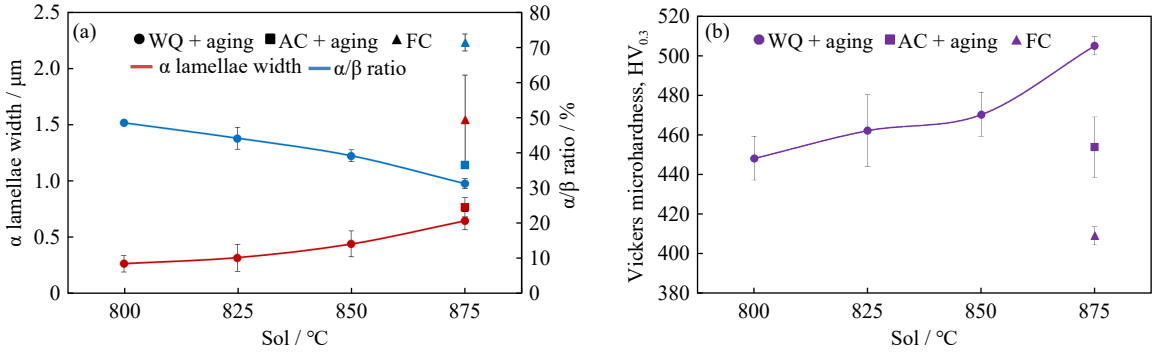

Fig. 9. (a) Influence of solution temperature and cooling mode on microstructural features with α/β ratio (blue) and α laths thickness (red) and (b) microhardness vs. solution temperature and cooling mode (violet).

aging (Fig. 10(a)), resulting in a maximum hardness of HV 506, which slightly decreased to HV 490 after 8 h of aging. These results were consistent with the findings of Galarraga *et al.* [41] and Yu *et al.* [42]. It is reasonable to assume that the unmarked reduction in hardness values could be attributed to the coarsening of Ti_3Al hardening precipitates. Still, this assumption could only be verified using transmission electron microscopy (TEM) analysis. Indeed, the microstructures of the samples subjected to treatments 875WQ_500_1 and 875WQ_500_8 (Fig. 10(b) and (c)) exhibited no noticeable differences, as confirmed by the results of the image analyses (Table 4). These analyses showed that the aging time had no appreciable influence on both the thickness of primary α lamellae and the α/β phase ratio.

According to the results of aging tests, 3 h of aging was considered the optimal compromise between achieving maximum strength and preventing underaging, particularly in the case of the heat treatment of large parts. Larger components required more time to reach the aging temperature than the smaller samples tested in this study.

Table 4 shows the microstructural and mechanical properties obtained after the various heat treatments performed.

3.2. Tensile tests and fracture surface analyses

The selection of heat treatments for further tensile testing focused on identifying those that could deliver both high mechanical strength and good toughness. Tensile tests were conducted on samples heat-treated according to the 875WQ_500_3 and 825WQ_500_3 parameters. The 875WQ_500_3 treatment resulted in a bilamellar microstructure with the highest hardness among the studied conditions, whereas the 825WQ_500_3 treatment produced a bilamellar microstructure with thinner primary α lamellae (0.31 vs. 0.64 μm) and maintained good hardness. The 875WQ_500_3 treatment was expected to ensure high tensile strength, whereas the 825WQ_500_3 treatment should provide a favorable balance between tensile strength and toughness/ductility.

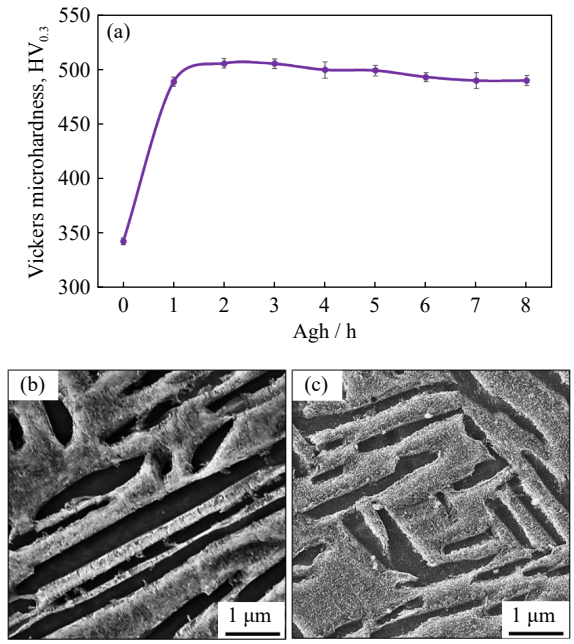

Fig. 10. (a) Hardness vs. aging time curve of samples solution-treated at 875°C, water quenched, and aged at 500°C; FE-SEM high-magnification images of (b) 875WQ_500_1 and (c) 875WQ_500_8 microstructures.

The results of the tensile tests are summarized in Table 5, whereas Fig. 11 presents a comparison of three nominal stress–strain curves representing three heat treatments. The STA heat treatments led to significantly higher YS and UTS compared with the 875FC treatment, with increases of 19% and 23% for 825WQ_500_3 and 38% and 39% for 875WQ_500_3, respectively. However, these gains were accompanied by a reduction in EL by about 55% for 825WQ_500_3 and 80% for 875WQ_500_3.

When comparing the tensile test results of the 825WQ_500_3 and 875WQ_500_3 samples with literature data [28–29,43], these new heat treatments evidently yielded higher strength and comparable ductility (particularly for the 825WQ_500_3 sample) compared with those reported for

Table 4. Microstructural (α/β ratio and α lamellae width) and mechanical (microhardness) properties obtained after different heat treatments

Designation	α/β ratio	α lamellae width / μm	Vickers microhardness, $HV_{0.3}$
800WQ_500_3	48.3 ± 0.8	0.26 ± 0.07	448 ± 11
825WQ_500_3	44.0 ± 3.1	0.31 ± 0.12	462 ± 18
850WQ_500_3	39.0 ± 1.6	0.43 ± 0.11	470 ± 11
875WQ_500_3	31.1 ± 1.5	0.64 ± 0.08	505 ± 5
875AC_500_3	36.4 ± 1.1	0.76 ± 0.09	454 ± 15
875FC	71.2 ± 2.4	1.54 ± 0.39	409 ± 5
875WQ	31.5 ± 0.7	0.70 ± 0.18	342 ± 3
875WQ_500_1	30.1 ± 0.9	0.65 ± 0.09	489 ± 4
875WQ_500_2	31.1 ± 0.8	0.66 ± 0.11	506 ± 6
875WQ_500_4	31.6 ± 0.9	0.70 ± 0.10	499 ± 8
875WQ_500_5	30.3 ± 1.4	0.63 ± 0.13	499 ± 5
875WQ_500_6	29.0 ± 1.2	0.61 ± 0.12	493 ± 4
875WQ_500_7	28.2 ± 1.1	0.61 ± 0.09	490 ± 7
875WQ_500_8	28.3 ± 0.9	0.60 ± 0.10	490 ± 7

Table 5. Summary of hardness and tensile properties evaluated on the investigated heat-treated Ti6246 samples

Designation	Vickers microhardness, $HV_{0.3}$	E / GPa	$R_{p0.2}$ / MPa	UTS / MPa	EL / %
875WQ_500_3	505 ± 5	118 ± 2	1289 ± 61	1509 ± 7	4.4 ± 0.8
825WQ_500_3	462 ± 18	118 ± 3	1118 ± 12	1327 ± 1	10.1 ± 0.4
875FC	410 ± 9	112 ± 1	936 ± 9	1085 ± 1	22.3 ± 0.5

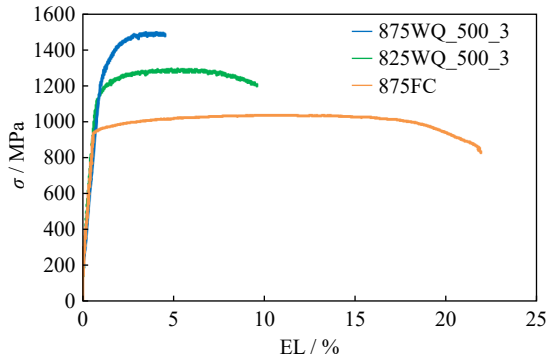

Fig. 11. Stress–strain curves of the heat-treated PBF–LB-produced Ti6246 samples.

PBF–LB-manufactured α–β titanium alloys. Moreover, the mechanical properties of the PBF–LB Ti6246 alloy after the optimized STA heat treatments were significantly enhanced compared with those reported for conventional manufactured alloy [27]. Specifically, the 825WQ_500_3 sample exhibited a 5% increase in UTS with comparable elongation to failure, whereas the 875WQ_500_3 sample demonstrated a 20% increase in UTS, though with a halving of elongation to failure.

These exceptional mechanical properties were attributed to the synergistic reinforcing effect of the bilamellar microstructure and the strengthening precipitates formed during the aging phase. The presence of an ultrafine lamellar structure combined with aging precipitates hindered dislocation movement, whereas the larger primary α lamellae contributed to maintaining the alloy's ductility, similar to the traditional bimodal microstructure of α–β alloys. The balance between the fractions of primary α lamellae and the ultrafine lamellar structure determined whether the material achieved higher strength with reduced ductility or a more balanced combination of both. Increasing the percentage of primary α lamellae and reducing their size enhanced ductility, whereas increasing the proportion of the ultrafine lamellar structure enhanced strength.

Fig. 12 presents representative images at various magnifications of the fracture surfaces from tensile specimens subjected to specified heat treatments. The fracture surfaces displayed a characteristic cup-and-cone morphology, typical of ductile fractures, featuring a central flat fibrous zone and a shear lip zone, as shown in Fig. 12(a)–(c), which was more pronounced as noted previously [44–45]. At high magnification, small gas pores (previously shown in Fig. 3(a)) and dimples were noticeable across all samples. However, the dimples differed in size and depth in the 875WQ_500_3 (Fig. 12(d) and (g)) and 825WQ_500_3 (Fig. 12(e) and (h)) samples, they were fine and shallow, whereas in the 875FC samples (Fig. 12(f) and (i)), the dimples were larger and deeper, coalescing and growing with increasing plastic strain. Additionally, in the 875WQ_500_3 samples, small areas of mixed brittle–ductile fracture were observed in regions with secondary cracks (Fig. 12(d)). These fracture morphologies correlated well with the previously discussed microstructure and the tensile test results. The STA-treated samples exhibited a finer microstructure, higher strength, and lower ductility compared with the annealed samples.

4. Conclusions

This investigation aimed at optimizing the STA process for the Ti6246 alloy manufactured using the PBF–LB technique yielded the following key conclusions:

(1) Solution treatment at 875°C followed by water quenching resulted in α–β lamellar microstructure devoid of α′ and α″ martensite. The subsequent aging treatment promoted the formation of a fully bilamellar microstructure characterized by the formation of secondary α lamellae within the β phase.

(2) The solution temperature significantly affected the alloy microstructure and mechanical properties. Higher solution temperatures led to the coarsening of α lamellae and a reduction in the α/β phase volume fraction. This increase in metastable β-phase content facilitated the formation of ultrafine secondary α lamellae and enhanced precipitation hardening during aging.

(3) The 875WQ_500_3 specimen exhibited the highest tensile strength, achieving a 39% increase over the 875FC sample, but exhibited 80% reduction in elongation to failure. In contrast, the 825WQ_500_3 treatment provided a favorable balance between strength and ductility, with only 12% decrease in tensile strength compared with the 875WQ_500_3 sample, while offering double the elongation to failure.

(4) The optimized STA treatment performed on the Ti6246 PBF–LB alloy showed 5% higher UTS compared with the same alloy produced using conventional methods.

This study addresses a notable gap in the literature concerning the optimization of heat treatments for PBF–LB Ti6246 alloys, paving the way for future industrial applications and better-performing components. Future work aims to involve additional investigations to assess the influence of the optimized heat treatment on the fatigue behavior of Ti6246 alloys compared with literature-based ones for comprehensive mechanical characterization.

Acknowledgements

This work was financed by the European Union – Next

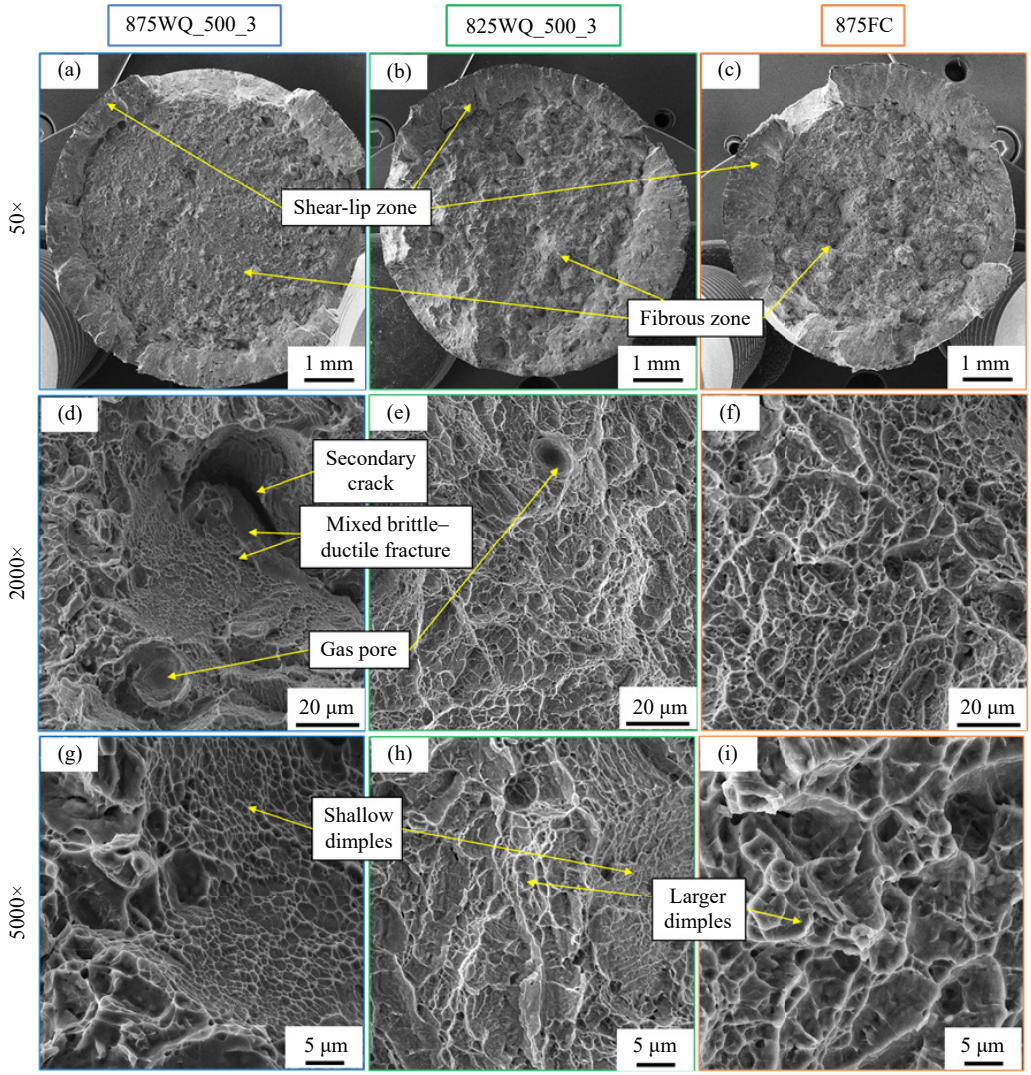

Fig. 12. FE-SEM images of the tensile fracture surfaces at different magnifications: (a, d, g) 875WQ_500_3; (b, e, h) 825WQ_500_3; (c, f, i) 875FC.

Generation EU (National Sustainable Mobility Center CN00000023, Italian Ministry of University and Research Decree n. 1033 - 17/06/2022, Spoke 11 - Innovative Materials & Lightweighting). The opinions expressed are those of the authors only and should not be considered representative of the European Union or the European Commission's official position. Neither the European Union nor the European Commission can be held responsible for them.

Conflict of Interest

The authors declare that they have no conflict of interest regarding the publication of this paper.

References

[1] H.Y. Fan, C.C. Wang, Y.J. Tian, K. Zhou, and S.F. Yang, Laser powder bed fusion (L-PBF) of Ti–6Al–4V/Ti–6Al–2Sn–4Zr–2Mo and Ti–6Al–4V/γ-TiAl bimetals: Processability, interface and mechanical properties, *Mater. Sci. Eng. A*, 871(2023), art. No. 144907.

[2] R.R. Boyer, Introduction and overview of titanium and titanium alloys, [in] J.R. Davis, eds., *Metals Handbook Desk Edition*, ASM International, Ohio State, 1998, p. 575.

[3] J.D. Destefani, Introduction to titanium and titanium alloys, [in] ASM Handbook Committee, *Properties and Selection*: *Nonferrous Alloys and Special-Purpose Materials*, ASM International, Ohio State, 1990, p. 586.

[4] C. Leyens and M. Peters, *Titanium and Titanium Alloys*: *Fundamentals and Applications*, Wiley-VCH, Berlin, 2003.

[5] G. Lütjering and J.C. Williams, *Titanium*, Springer, Berlin, 2007, p. 337.

[6] M.M. Attallah, S. Zabeen, R.J. Cernik, and M. Preuss, Comparative determination of the α/β phase fraction in α + β-titanium alloys using X-ray diffraction and electron microscopy, *Mater. Charact.*, 60(2009), No. 11, p. 1248.

[7] A. Carrozza, A. Aversa, P. Fino, and M. Lombardi, A study on the microstructure and mechanical properties of the Ti–6Al–2Sn–4Zr–6Mo alloy produced *via* laser powder bed fusion, *J. Alloys Compd.*, 870(2021), art. No. 159329.

[8] G.X. Li, S. Chandra, R.A.R. Rashid, S. Palanisamy, and S.L. Ding, Machinability of additively manufactured titanium alloys: A comprehensive review, *J. Manuf. Process.*, 75(2022), p. 72.

[9] H.D. Nguyen, A. Pramanik, A.K. Basak, *et al.*, A critical review on additive manufacturing of Ti–6Al–4V alloy: Microstructure and mechanical properties, *J. Mater. Res. Technol.*, 18(2022), p. 4641.

[10] S.Y. Liu and Y.C. Shin, Additive manufacturing of Ti_6Al_4V al-

loy: A review, *Mater. Des.*, 164(2019), art. No. 107552.
[11] P. Nyamekye, S.R. Golroudbary, H. Piili, P. Luukka, and A. Kraslawski, Impact of additive manufacturing on titanium supply chain: Case of titanium alloys in automotive and aerospace industries, *Adv. Ind. Manuf. Eng.*, 6(2023), art. No. 100112.
[12] S. Cecchel, Materials and technologies for lightweighting of structural parts for automotive applications: A review, *SAE Int. J. Mater. Manf.*, 14(2020), No. 1, p. 5.
[13] M. Motyka, Martensite formation and decomposition during traditional and AM processing of two-phase titanium alloys–An overview, *Metals*, 11(2021), No. 3, art. No. 481.
[14] D. Herzog, V. Seyda, E. Wycisk, and C. Emmelmann, Additive manufacturing of metals, *Acta Mater.*, 117(2016), p. 371.
[15] S. Alipour, A. Moridi, F. Liou, and A. Emdadi, The trajectory of additively manufactured titanium alloys with superior mechanical properties and engineered microstructures, *Addit. Manuf.*, 60(2022), art. No. 103245.
[16] A. Carrozza, A. Aversa, P. Fino, and M. Lombardi, Towards customized heat treatments and mechanical properties in the LPBF-processed Ti–6Al–2Sn–4Zr–6Mo alloy, *Mater. Des.*, 215(2022), art. No. 110512.
[17] H.K. Rafi, N.V. Karthik, H.J. Gong, T.L. Starr, and B.E. Stucker, Microstructures and mechanical properties of Ti_6Al_4V parts fabricated by selective laser melting and electron beam melting, *J. Mater. Eng. Perform.*, 22(2013), No. 12, p. 3872.
[18] A. Takase, Residual stress and phase stability of titanium alloys fabricated by laser and electron beam powder bed fusion techniques, *Mater. Trans.*, 64(2023), No. 1, p. 17.
[19] Z.X. Xiao, C.P. Chen, H.H. Zhu, *et al*., Study of residual stress in selective laser melting of Ti_6Al_4V, *Mater. Des.*, 193(2020), art. No. 108846.
[20] N. Yumak and K.Aslantas, A review on heat treatment efficiency in metastable β titanium alloys: The role of treatment process and parameters, *J. Mater. Res. Technol.*, 9(2020), No. 6, p. 15360.
[21] R.P. Kolli and A. Devaraj, A review of metastable beta titanium alloys, *Metals*, 8(2018), No. 7, art. No. 506.
[22] C. Sauer and G. Lütjering, Processing, microstructure and properties of Ti-6246, [in] *Proceedings of the 9th World Conference on Titanium*: *Titanium*, Saint-Petersburg, 1999.
[23] J.D. Cotton, R.D. Briggs, R.R. Boyer, *et al*., State of the art in beta titanium alloys for airframe applications, *JOM*, 67(2015), No. 6, p. 1281.
[24] R. Santhosh, M. Geetha, and M.N. Rao, Recent developments in heat treatment of beta titanium alloys for aerospace applications, *Trans. Indian Inst. Met.*, 70(2017), No. 7, p. 1681.
[25] A. Gheysarian and M. Abbasi, The effect of aging on microstructure, formability and springback of Ti–6Al–4V titanium alloy, *J. Mater. Eng. Perform.*, 26(2017), No. 1, p. 374.
[26] M. Jackson, R.J. Dashwood, L. Christodoulou, and H.M. Flower, Isothermal subtransus forging of Ti–6Al–2Sn–4Zr–6Mo, *J. Light. Met.*, 2(2002), No. 3, p. 185.
[27] M.H.I. Alluaibi, E.M. Cojocaru, A. Rusea, N. Șerban, G. Coman, and V.D. Cojocaru, Microstructure and mechanical properties evolution during solution and ageing treatment for a hot deformed, above β-transus, Ti-6246 alloy, *Metals*, 10(2020), No. 9, art. No. 1114.
[28] H.C. Yu, F.Z. Li, Z.M. Wang, and X.Y. Zeng, Fatigue performances of selective laser melted Ti–6Al–4V alloy: Influence of surface finishing, hot isostatic pressing and heat treatments, *Int. J. Fatigue*, 120(2019), p. 175.
[29] G. Ter Haar and T. Becker, Selective laser melting produced Ti–6Al–4V: Post-process heat treatments to achieve superior tensile properties, *Materials*, 11(2018), No. 1, art. No. 146.
[30] R. Casati, G. Boari, A. Rizzi, and M. Vedani, Effect of annealing temperature on microstructure and high-temperature tensile behaviour of Ti-6242S alloy produced by laser powder bed fusion, *Eur. J. Mater.*, 1(2021), No. 1, p. 72.
[31] C. Fleißner-Rieger, T. Pfeifer, C. Turk, and H. Clemens, Optimization of the post-process heat treatment strategy for a near-α titanium base alloy produced by laser powder bed fusion, *Materials*, 15(2022), No. 3, art. No. 1032.
[32] Y. Chong, T. Bhattacharjee, and N. Tsuji, Bi-lamellar microstructure in Ti–6Al–4V: Microstructure evolution and mechanical properties, *Mater. Sci. Eng. A*, 762(2019), art. No. 138077.
[33] S. Lampman, Wrought titanium and titanium alloys, [in] ASM Handbook Committee, *Properties and Selection*: *Nonferrous Alloys and Special-Purpose Materials*, ASM International, Ohio State, 1990, p. 592.
[34] R. Gaddam, B. Sefer, R. Pederson, and M.L. Antti, Study of alpha-case depth in Ti–6Al–2Sn–4Zr–2Mo and Ti–6Al–4V, *IOP Conf. Ser.*: *Mater. Sci. Eng.*, 48(2013), art. No. 012002.
[35] P. Stella, I. Giovanetti, G. Masi, M. Leoni, and A. Molinari, Microstructure and microhardness of heat-treated Ti–6Al–2Sn–4Zr–6Mo alloy, *J. Alloys Compd.*, 567(2013), p. 134.
[36] A.L. Otte, P.T. Mai, A. Stark, M. Hoelzel, M. Hofmann, and J. Gibmeier, Kinetics of martensite decomposition and microstructure stability of Ti-6246 during rapid heating to service temperatures, *Metals*, 13(2023), No. 3, art. No. 484.
[37] Y. Vahidshad and A.H. Khodabakhshi, Effect of solution treatment and aging temperature on α' and Ti_3Al(α2) phase formation and mechanical properties of water-quenched Ti–6Al–4V, *Metallogr. Microstruct. Anal.*, 11(2022), No. 1, p. 59.
[38] L.M. Gammon, R.D. Briggs, J.M. Packard, K.W. Batson, R. Boyer, and C.W. Domby, Metallography and microstructures of titanium and its alloys, [in] G.F.V. Voor, eds., *Metallography and Microstructures*, ASM International, Ohio State, 2004, p. 899.
[39] M. Villa, J.W. Brooks, R.P. Turner, H. Wang, F. Boitout, and R.M. Ward, Microstructural modeling of the α + β phase in Ti–6Al–4V: A diffusion-based approach, *Metall. Mater. Trans. B*, 50(2019), No. 6, p. 2898.
[40] S. Malinov, W. Sha, Z. Guo, C.C. Tang, and A.E. Long, Synchrotron X-ray diffraction study of the phase transformations in titanium alloys, *Mater. Charact.*, 48(2002), No. 4, p. 279.
[41] H. Galarraga, R.J. Warren, D.A. Lados, R.R. Dehoff, M.M. Kirka, and P. Nandwana, Effects of heat treatments on microstructure and properties of Ti–6Al–4V ELI alloy fabricated by electron beam melting (EBM), *Mater. Sci. Eng. A*, 685(2017), p. 417.
[42] J.X. Yu, Z.P. Yin, Z.R. Huang, *et al*., Effect of aging treatment on microstructural evolution and mechanical properties of the electron beam cold hearth melting Ti–6Al–4V alloy, *Materials*, 15(2022), No. 20, art. No. 7122.
[43] H. Jaber, J. Kónya, K. Kulcsár, and T. Kovács, Effects of annealing and solution treatments on the microstructure and mechanical properties of Ti_6Al_4V manufactured by selective laser melting, *Materials*, 15(2022), No. 5, art. No. 1978.
[44] W.T. Becker, Mechanisms and appearances of ductile and brittle fracture in metals, [in] W.T. Becker and R.J. Shipley, eds., *Failure Analysis and Prevention*, ASM International, Ohio State, 2002, p. 587.
[45] V.A. Joshi, Titanium alloys: Atlas of fractographs, [in] ASM Handbook Committee, *Fractography*, ASM International, Ohio State, 1987, p. 441.